An unsteady stall-delay methodology for floating offshore wind turbines

ABDULQADIR AZIZ SINGAPORE WALA
Nanyang Technological University
School of Mechanical and
Aerospace Engineering
50 Nanyang Ave, Block N3,
Nanyang Ave, Singapore 639798
SINGAPORE
abdulqadir.aziz@gmail.com

EDDIE YK NG
Nanyang Technological University
School of Mechanical and
Aerospace Engineering
50 Nanyang Ave, Block N3,
Nanyang Ave, Singapore 639798
SINGAPORE
MYKNG@NTU.edu.sg

NARASIMALU SRIKANTH
Nanyang Technological University
Energy Research Institute @ NTU
50 Nanyang Dr, Singapore 637553
SINGAPORE
nsrikanth@NTU.edu.sg

ANAND BAHUGUNI
Lloyd's Register
Global Technology Centre
1 Fusionopolis Place, # 09-01,
Singapore 138522
SINGAPORE
anand.bahuguni@lr.org

Abstract: Stall-delay is a known phenomenon in wind turbines, and has been associated with the Coriolis effect along the blade, which contributes to the suppression of flow separation. Floating offshore wind turbines (FOWTs) operate in unsteady environments due to 6 degree-of-freedom platform motions. This results in unsteady airfoil effects and a non-static stall delay effect that would be in constant flux due to he changing tip speed ratio of the wind turbine. To ensure an accurate assessment of wind turbine aerodynamics, the stall delay effect needs to be accounted for at every time step, and not before a computation is performed as is traditionally done for wind turbine aerodynamics computation using BEM. The commonly used Beddoes-Leishman model for unsteady airfoil effects, however, is based on static aerodynamics data, but this would be constantly changing with a changing stall-delay. Thus, a combined Beddoes-Leishman and Du & Selig model is proposed to reconcile the shifting static aerodynamics coefficients of the airfoil cross-sections of wind turbine blades with the unsteady airfoil effect.

Key–Words: stall delay, unsteady airfoil, unsteady aerodynamic, Beddoes-Leishman, Du & Selig, dynamic stall, floating offshore wind turbines

1 Introduction

All computational methods in wind turbine aerodynamics, short of a full 3D computational fluid dynamics simulation by creation of a suitably fine computational grid around the rotor geometry, would require the determination of the local cross-sectional aerodynamics based on present flow conditions at the particular rotor station. This is done through a simple lookup table for the generally steady aerodynamics found in fixed-bottom rotors, while it is modelled using an appropriate unsteady aerodynamics model for the unsteady aerodynamics generally found in floating offshore wind turbines (FOWTs) due to the 6 degree of freedom platform motions. However, using 2-dimensional airfoil data in these applications would be erroneous, given that the radial flows due to the rotation of the rotor result in significant stall delay in the rotor blades. This effect has been shown to be most significant at tip speed ratios (TSR) lower than 3.0 [1].

A stall delay model is needed to correct for the position of flow separation in the unsteady airfoil model based on the Kirchoff equation [2]. This is generally accounted for by means of correction to the static aerodynamics table before performing a simulation or analysis, since for most wind turbines, the operating TSR is known beforehand. For FOWTs however, the TSR is constantly changing as the relative wind changes periodically based on platform motions. This means that the stall delay effect would constantly be changing over the rotor blade during operation. Thus, the stall delay model needs to be

constantly called during operation and combined with the unsteady aerodynamics model for an improved description of FOWT blade cross-sectional aerodynamics.

This paper will present a combined stall-delay and unsteady airfoil model, by implementing the Du & Selig [3] model for stall-delay and modified Beddoes-Leishman model of Singapore Wala et al [4] for unsteady airfoil aerodynamics in a manner that will take into account the changing local speed ratio of the FOWT blade cross-section. This model will be implemented in the unsteady blade element momentum uBEM method of Singapore Wala et al then compared to full 3D CFD simulations of the NREL 5MW virtual wind turbine in surge motion. These comparisons will show a significant improvement in modelling accuracy by accounting for changes in TSR during operation.

2 Model descriptions

2.1 Du & Selig stall delay model [3]

The Du & Selig model [3] is based on the Coriolis effect on 3D boundary layers over the blade. The equations correct the 2D coefficients of lift and drag to account for the stall delay.

$$C_l^{sd}(\alpha) = g \cdot C_{l\alpha} \cdot (\alpha - \alpha_0) + (1-g) \cdot C_{l,2D} \quad (1)$$

$$C_d^{sd}(\alpha) = gd \cdot C_{d0} + (1-gd) \cdot C_{d,2D} \quad (2)$$

where $C_{l\alpha}$ is the lift curve slope from 2D data, $C_{l,2D}$ is the 2D coefficient of lift, α_0 is the angle of attack at zero lift, $C_{d,2D}$ is the 2D coefficient of drag and C_{d0} is the coefficient of drag at zero lift. g and gd are flow separation point functions given by:

$$g = \frac{1}{2\pi} \cdot \left(\frac{1.6\,(c/r) - (c/r)^{\Lambda}}{0.1267 + (c/r)^{\Lambda}} - 1 \right) \quad (3)$$

$$gd = \frac{1}{2\pi} \cdot \left(\frac{1.6\,(c/r) - (c/r)^{\Lambda/2}}{0.1267 + (c/r)^{\Lambda/2}} - 1 \right) \quad (4)$$

where c is the chord length at the local blade station, r is the local radius, and Λ is the inverse of the local speed ratio given by:

$$\Lambda = \frac{V_{rel,wind}}{V_{rot}} \quad (5)$$

where $V_{rel,wind}$ is the total relative wind velocity at the blade section, and V_{rot} is the rotational wind velocity at the blade section.

g and gd are set to 0 when the angle of attack exceeds 30° [5] or is below -20°.

Since Λ is expected to change with time in a FOWT, the Du & Selig model cannot be pre-applied to 2D aerodynamic data for airfoils.

2.2 Beddoes-Leishman unsteady airfoil model [6]

The Beddoes-Leishman model presented here is based on the the implementation by Singapore Wala et al [4].

A non-dimensionalised time, s is defined for time step n.

$$s_{(n)} = \frac{2V_\infty \cdot t_{(n)}}{c} \quad (6)$$

where V_∞ is the freestream velocity, $t_{(n)}$ is the time at time step n and c is the airfoil chord length.

2.2.1 Unsteady attached flow

The unsteady attached flow is computed by defining an effective angle of attack for the unsteady airfoil [4].

$$\alpha_E = \alpha_n - X(s) \quad (7)$$

where $X(s)$ is an indicial function of non-dimensional time, s, defined as:

$$X\left(s_{(n)}\right) = X\left(s_{(n-1)}\right) \exp\left(b_1\left(\Delta s_{(n)}\right)\right) + A_1 \cdot \Delta\alpha_{(n)} \cdot \exp\left(\frac{-b_1 \cdot \Delta s_{(n)}}{2}\right) \quad (8)$$

Δ refers to the change in the parameter from the previous time step. A_1 and b_1 are dimensionless constants.

The circulatory attached flow lift is then computed using:

$$C_L^C = C_{L\alpha} \cdot (\alpha_E - \alpha_0) \quad (9)$$

where $C_{L\alpha}$ is the lift curve slope in the linear region of the lift curve and α_0 is the angle of attack of zero lift. By the Kelvin theorem, the total circulation must remain constant. This is possible by shed vorticity when there is a change in the angle of attack. The shed vorticity results in a reduction of the effective change in angle of attack.

The impulsive lift is given by:

$$C_{L(n)}^I = \frac{4 \cdot K_\alpha \cdot c}{V_\infty^2} \cdot \left(\frac{\Delta u_{p(n)} - \Delta u_{p(n-1)}}{\Delta t} - D_{(n)} \right) \quad (10)$$

where K_α is a dimensionless constant related to Mach number, set to 0.846 for a Mach number of 0.15, as described in [7]. u_p is the plunge velocity given by [7]:

$$u_p = V_\infty(\Delta\alpha) + \alpha(\Delta V_{\infty(n)}) \tag{11}$$

where $\Delta V_{\infty(n)}$ is the change in freestream velocity from the previous time step and $D_{(n)}$ is the deficiency function given by:

$$D_{(n)} = D_{(n-1)}exp\left(\frac{-\Delta t}{K_\alpha \cdot T_I}\right) + \left(\frac{\Delta u_{p(n)} - \Delta u_{p(n-1)}}{\Delta t}\right) exp\left(\frac{-\Delta t}{2K_\alpha \cdot T_I}\right) \tag{12}$$

The impulsive lift can be described as an added-mass lift, as it is resultant from the reaction of the air accelerating around a plunging airfoil. A detailed description is provided in [4].

The total unsteady attached flow lift, or potential flow lift is given by:

$$C_L^P = C_L^C + C_L^I \tag{13}$$

2.2.2 Unsteady trailing edge separation

The unsteady attached flow lift, as described by [8] requires defining the point of flow separation under steady state conditions. This is done using the equation for lift on a flat plate in a potential Kirchoff flow [9]. The point of flow separation for an airfoil in steady-state flow is defined at each angle of attack:

$$f^{st} = \left(2\sqrt{\frac{C_L^{st}(\alpha)}{C_{L\alpha}\cdot(\alpha-\alpha_0)}} - 1\right)^2 \tag{14}$$

where C_L^{st} is the steady-state lift.

f^{st} is set to zero (fully separated flow) at angles of attack where the value of f^{st} derived from equation (14) does not retrieve the static lift coefficient:

$$C_L^{st} \neq \left(\frac{1+\sqrt{f^{st}(\alpha)}}{2}\right)^2 \cdot (\alpha - \alpha_0) \tag{15}$$

Using experimental lift curves, $C_{L\alpha}$ is taken to be the maximum lift curve value from the set of measured lift coefficients:

$$C_{L\alpha} = max\left(\frac{C_L^{st}(\alpha)}{\alpha-\alpha_0}\right) \tag{16}$$

The flow separation over an airfoil is dependent on pressure distribution, which is related to lift [8]. There is a time lag between this pressure response and the lift, and this time lag is modelled through a further time lag to the unsteady attached flow lift:

$$C_L'^P = C_L^P - D_P \tag{17}$$

D_P is a deficiency function given by:

$$D_{P(n)} = D_{P(n-1)}exp\left(\frac{-\Delta s_{(n)}}{T_P}\right) + (C_{L(n)}^P - C_{L(n-1)}^P)exp\left(\frac{-\Delta s_{(n)}}{2\cdot T_P}\right) \tag{18}$$

where T_P is a time constant.

This time-lagged unsteady attached flow lift is used to find a new effective angle of attack:

$$\alpha_f = \frac{C_L'^P}{C_{L\alpha}} - \alpha_0 \tag{19}$$

The position of flow separation based on the new effective angle of attack is looked up from the static data table:

$$f' = f(\alpha_f) \tag{20}$$

The time lag between the unsteady pressure response and the position of flow separation is modelled to find a dynamic position of flow separation.

$$f^{dyn} = f' - D_f \tag{21}$$

D_f is the deficiency function given by:

$$D_{f(n)} = D_{f(n-1)}exp\left(\frac{-\Delta s_{(n)}}{T_f}\right) + (f_{\mathrm{FL}(n)} - f_{\mathrm{FL}}(n-1))exp\left(\frac{-\Delta s_{(n)}}{2\cdot T_f}\right) \tag{22}$$

where T_f is a constant.

In equation (21), the dynamic position of flow separation (with respect to the airfoil chord) is modelled with the assumption of a time lag between dynamic flow separation and the flow separation based on the unsteady pressure response on the airfoil. The flow separation based on the unsteady pressure response on the airfoil is found using a look-up table of static positions of flow separation with the effective angle of attack derived from the time-lagged unsteady attached flow lift. The time lag is modelled using the deficiency function in equation (22) with a time constant of T_f.

The total dynamic lift with trailing edge separation is then found using the equation for lift on a flat plate in a potential Kirchoff flow [9]:

$$C_L^f = \left(\frac{1+\sqrt{f^{dyn}}}{2}\right)^2 \cdot (\alpha_E - \alpha_0) \tag{23}$$

When $f^{dyn} = 0$, this is set to:

$$C_L^f = C_L^{st}(\alpha_E) \tag{24}$$

The circulation of an airfoil is linearly related to the lift produced, not angle of attack, since the lift and angle of attack do not share a linear relationship when there is flow separation. Thus, equations (6) to (25) are used as an initial estimate of C_L^f, to find the change in circulatory angle of attack, $\Delta\alpha_c$.

$$\Delta\alpha_c = \frac{C_{L(n)}^f - C_{L(n-1)}^f}{C_{L\alpha}} \tag{25}$$

$\Delta\alpha_c$ then replaces $\Delta\alpha$ in equation (8), and equations (6) to (25) are repeated to find C_L^f.

2.2.3 Vortex lift

Vortex lift refers to the dynamic stall phenomenon, where leading edge separation causes the propagation of a vortex over the suction surface of the airfoil, resulting in a momentary increase in lift. While the leading edge separation onset criterion has been discussed, and has been based on the potential flow lift exceeding a certain value [10], this criterion does not need to be applied explicitly, and can instead be applied when the feed to the vortex lift exceeds zero [7]. The feed for the vortex lift is modelled using the difference between circulatory attached flow lift and dynamic lift with trailing edge separation:

$$\Delta c_v = c_{v(n)} - c_{v(n-1)} \tag{26}$$

$$c_v = C_L^C - C_L^f \tag{27}$$

The vortex lift, C_L^v is then:

$$C_{L(n)}^v = C_{L(n-1)}^v \cdot exp\left(\frac{-\Delta s_{(n)}}{T_v}\right) + \Delta c_v \cdot exp\left(\frac{-\Delta s_{(n)}}{2 \cdot T_v}\right) \tag{28}$$

where T_v is a constant. This is set to zero if the feed to the vortex lift is negative, the angle of attack is increasing, or exceeds 50° [7].

The total unsteady lift is then:

$$C_L^{dyn} = C_L^I + C_L^f + C_L^v \tag{29}$$

2.2.4 Drag and moment components

The unsteady drag is modelled as an additional unsteady component to static drag, based on parameters predicted during the computation of dynamic lift [8].

$$C_D^{dyn} = C_D^{st}(\alpha_E) + C_L^{dyn} \cdot (\alpha - \alpha_E) + \left(C_D^{st}(\alpha_E)\right) \cdot \left(\left(\frac{1-\sqrt{f^{dyn}}}{2}\right)^2 - \left(\frac{1-\sqrt{f^{st}(\alpha_E)}}{2}\right)^2\right) \tag{30}$$

The dynamic moment includes additional components based on impulsive lift [7].

$$C_M^{dyn} = C_M^{st}(\alpha_E) - \frac{C_L^I}{4} \tag{31}$$

2.2.5 Model constants

As presented in [4], the model constants can be optimised based on airfoil shape, and models were formed to equate the constants to shape parameters based on a simplified round-nosed, sharp trailing-edged shape representation of the suction surface of the airfoil:

$$z = \tau \cdot \sqrt{\frac{x}{c}} \cdot \left(1 - \frac{x}{c}\right) \cdot \left(1 - A \cdot \left(\frac{x}{c}\right)\right) \tag{32}$$

In equation (32), A is a curvature parameter that determines the general shape of the curve, while τ is a thickness parameter that determines the thickness of the airfoil. Expanding the equation shows that τA would also be an important parameter for the airfoil shape, which takes into account both curvature and thickness. The closest matches between equation (32) and the suction surface shape of the NREL 5MW blade cross-sectional profiles were used, with the parameters τ, A and τA used to find the optimal constants. The shape-based equations for each dimensionless constant are presented in Table 1.

Table 1: Suction surface shape-dependent values of constants in Beddoes-Leishman model after final optimisation

Constant	Value
A_1	0.93
b_1	0.52
K_α	-64.4$(\tau A)^2$ - 2.7τA + 0.8
T_P	72.8τ^2 - 45.1τ + 7.0
T_f	-260.7$(\tau A)^2$ - 21.3τ A + 6.5
T_V	22.5A^2 + 9.3A + 2.3

2.3 Combined Stall-Delay and Unsteady Airfoil Model

A combined model for application in fully-coupled models for FOWTs would require several properties. Firstly, the periodically changing local wind conditions at each blade station due to platform motions, and the possible addition of a control module to simulate changes in the rotor RPM, would result in changing local wind conditions as well as TSR, resulting in constantly changing Reynolds numbers, unsteady airfoil effects and stall delay. The combined model must thus be able to interpolate between data of several Reynolds numbers as well as account for the changing stall delay. Secondly, the model must use 2D static airfoil lift and drag data, so that the information input into wind turbine aerodynamics models at present would be enough for the current model.

An important feature of the Du & Selig stall delay model [3] is that the lift curve slope of the linear portion of the lift curve does not change. This is an input parameter for the Beddoes-Leishman model, and can be predetermined from the 2D airfoil data. This will facilitate the interpolation of the data from datasets of different flow Reynolds numbers.

2.3.1 Stall-delayed unsteady lift

At a given flow condition, the flow velocity is used to determine the Reynolds number, based on which the $C_{l\alpha}$, α_0 and C_{d0} are interpolated from the 2 closest Re datasets available.

$$C_{l\alpha} = C_{l\alpha}\left(Re\right) \tag{33}$$

$$\alpha_0 = \alpha_0\left(Re\right) \tag{34}$$

$$C_{d0} = C_{d0}\left(Re\right) \tag{35}$$

α_f, the new effective angle of attack based on time-lagged unsteady attached flow lift, is obtained using equation (19). Equation (1) is then applied at α_f, and the stall-delayed static coefficient of lift, $C_L^{sd}\left(\alpha_f\right)$ is obtained and then used to find the position of flow separation at α_f, f_{FL}.

$$f_{\mathrm{FL}} = \left(2\sqrt{\frac{C_L^{sd}\left(\alpha_f\right)}{C_{L\alpha}\cdot\left(\alpha_f-\alpha_0\right)}}-1\right)^2 \tag{36}$$

If the derived value of f_{FL} does not retrieve $C_L^{sd}\left(\alpha_f\right)$, it is set to 0.

$$f_{\mathrm{FL}} = \begin{cases} f_{\mathrm{FL}}, & \text{if } C_L^{sd}\left(\alpha_f\right) = \\ & C_{L\alpha}\left(\frac{1+\sqrt{f_{\mathrm{FL}}\left(\alpha_f\right)}}{2}\right)^2\left(\alpha_f-\alpha_0\right) \\ 0, & \text{otherwise} \end{cases} \tag{37}$$

Equation (37) is used in (21) to (24) are then applied to find the dynamic position of flow separation, f^{dyn}, using which the dynamic coefficient of lift with trailing edge separation, C_L^f is found. if $f^{dyn}=0$, then C_L^f is set to the stall-delayed coefficient of lift based on the effective angle of attack:

$$C_L^f = \begin{cases} C_{L\alpha}\left(\frac{1+\sqrt{f^{dyn}}}{2}\right)^2\cdot \\ \left(\alpha_E-\alpha_0\right), & \text{if } f^{dyn}>0 \\ C_L^{sd}\left(\alpha_E\right), & \text{otherwise} \end{cases} \tag{38}$$

Vortex lift, caused by leading-edge flow separation is also affected by stall-delay, since the separation at the leading-edge is also delayed by the radial flows over the blade. As shown in equations (26) and (27), the feed of the vortex lift is based on the difference between circulatory lift and stall-delayed dynamic coefficient of lift with trailing edge separation.

2.3.2 Stall-delayed unsteady drag

The stall-delayed static coefficient of drag, $C_D^{sd}\left(\alpha_E\right)$, can be determined by finding the coefficient of drag from 2D data and applying equation (2). After which, the static position of flow separation at α_E, $f^{st}(\alpha_E)$, may be found using:

$$f^{st} = \left(2\sqrt{\frac{C_L^{sd}\left(\alpha_E\right)}{C_{L\alpha}\cdot\left(\alpha_E-\alpha_0\right)}}-1\right)^2 \tag{39}$$

The equation (37) is reapplied for f^{st} to determine if the flow has fully separated:

$$f^{st} = \begin{cases} f^{st}, & \text{if } C_L^{sd}\left(\alpha_E\right) = 0.25\cdot C_{L\alpha}\cdot \\ & \left(\frac{1+\sqrt{f^{st}(\alpha_E)}}{2}\right)^2\cdot\left(\alpha_E-\alpha_0\right) \\ 0, & \text{otherwise} \end{cases} \tag{40}$$

The stall-delayed unsteady coefficient of drag, ,

$C_D^{sd,dyn}$ is then found using:

$$C_D^{sd,dyn} = C_D^{sd}(\alpha_E) + C_L^{dyn} \cdot (\alpha - \alpha_E) + \left(C_D^{sd}(\alpha_E)\right) \cdot \left(\left(\frac{1-\sqrt{f^{dyn}}}{2}\right)^2 - \left(\frac{1-\sqrt{f^{st}(\alpha_E)}}{2}\right)^2\right) \quad (41)$$

The Du & Selig model does not correct the coefficient of moment of the airfoil, thus, the unsteady moment from the unsteady airfoil model, equation (31) would be used instead.

3 Methodology

The modelling methodology used for CFD and uBEM was presented in [11] and [12], and repeated here for ease of reference.

3.1 Simulation matrix

A total of 9 simulations were conducted, with sinusoidal surge motions at 3 different frequencies and 3 different amplitudes. The simulated wind speed was 10m/s at 11.45RPM. The surge motion frequencies and amplitudes are summarized in Table 2.

Table 2: Sinusoidal surge motion amplitudes and frequencies in present study

Amplitudes (m)	**Frequencies (Hz)**
2, 4, 6	0.02, 0.10, 0.50

3.2 Computational Fluid Dynamics

The CFD simulations were performed in ANSYS CFX 16. A single blade was used in 120° periodic simulations to reduce computational time. A frozen rotor approach was employed to simulate the rotation of the blade. The $k-\omega$ SST turbulence model was used with 5% turbulence intensity. The fluid was standard air at 25°C. A high resolution scheme was used for advection and turbulence numerics, while a second-order back Euler scheme was used for time-stepping. A fourth order Rhie-Chow interpolation was used for pressure-velocity coupling. The inlet boundary was a velocity inlet with uniform velocity of 10m/s, and the outlet was a pressure outlet with a gauge pressure of 0Pa. The far-field boundaries were set as openings, while the blade was a no-slip wall.

3.2.1 Mesh setup

The mesh was divided into 3 regions: Blade, Near-wake and Far-wake. The blade region was situated directly around the blade, in an o-grid. The height of the first layer of the blade was 6.6μm to 8.2μm, depending on position along the blade. This is shown in Figure 1.

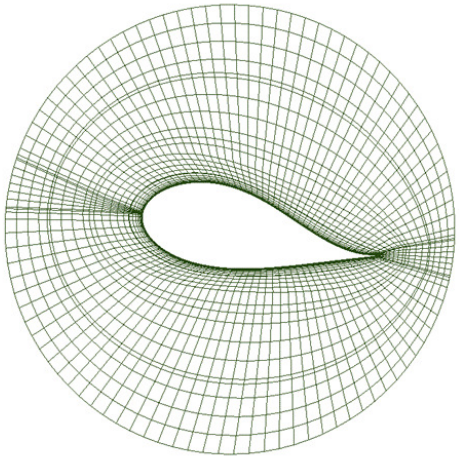

Figure 1: O-grid generated around the rotor blade

The mesh was refined to ensure that y+$<$1 over most of the blade, as shown in Figure 2. The y+ only exceeds 1 near the tip, but is still low at y+=3.

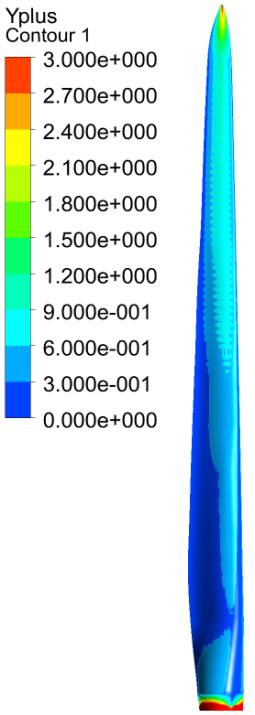

Figure 2: y+ over blade during static simulation

The near-wake region is a cylindrical region of refined mesh to ensure that the flow features of the near-wake a satisfactorily resolved for the accurate determination of blade forces. The near-wake mesh region extends 1R, or 1 rotor-radius upstream and 3.33R downstream of the rotor. The radius of the near-wake region extends 1.17R in the radial direction. The near wake and blade regions were set to rotate at 11.45 RPM in the frozen rotor approach.

The far-wake region extends 4.8R upstream and 11R downstream of the rotor. It extends 6R in the radial direction. The near-wake and far-wake regions are shown in Figures 3 and 4.

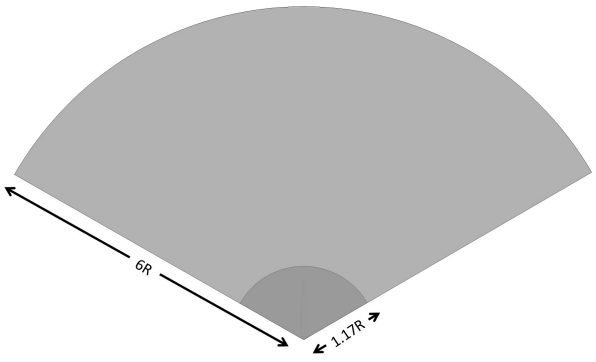

Figure 3: Front view of computational domain

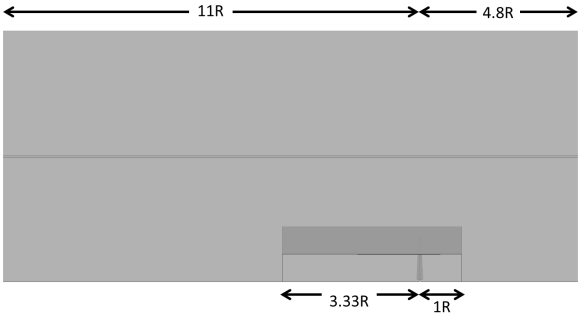

Figure 4: Side view of computational domain

A deforming mesh was used to simulate the rotor surge motion. The near-wake and blade regions were given a high mesh rigidity, thus deformation was limited to the far-wake region, to prevent negative volumes. The surge motion was defined by the equation:

$$S = -A + A\cos(2\pi f) \tag{42}$$

where S is the displacement of the rotor, A is the amplitude of motion and f is the frequency of motion.

3.2.2 Mesh Refinement

A mesh refinement study was carried out with a coarse (3.3 million cells), medium, (3.7 million cells) and fine (6 million cells) mesh. The mesh refinement was performed on a static rotor, then on 2 cases of sinusoidal surge motions with amplitudes and frequencies shown in Table 3.

Table 3: Sinusoidal surge conditions in mesh refinement study

Amplitude (m)	Frequency (Hz)
2	0.02
4	0.10

The percentage differences in elemental thrust and shaft torque from the medium mesh, for the coarse and fine meshes, in the static case, are recorded in Table 4.

Table 4: Percentage change in thrust and shaft torque at each blade segment, compared to medium mesh for static simulation

	Thrust (%)		Torque(%)	
r/R	coarse	fine	coarse	fine
0.19	3.02	1.05	2.18	0.81
0.25	0.29	0.14	0.28	0.15
0.32	0.01	0.00	0.02	0.05
0.38	0.03	0.06	0.04	0.08
0.45	0.00	0.09	0.03	0.10
0.51	0.00	0.00	0.01	0.10
0.58	0.00	0.07	0.00	0.08
0.64	0.00	0.00	0.01	0.07
0.71	0.00	0.00	0.01	0.09
0.77	0.00	0.00	0.00	0.10
0.84	0.00	0.05	0.00	0.09
0.89	0.00	0.00	0.04	0.06
0.93	0.00	0.00	0.02	0.08
0.98	0.01	0.02	0.02	0.07

The forces at each element had a maximum difference of 1.05% for thrust and 0.81% for torque between the medium and fine meshes. Thus, the medium mesh was deemed sufficiently refined for the static rotor. The time step for the dynamic simulations was $\Delta T = 1/(200f)$, meaning 200 timesteps per oscillatory period. The percentage error in rotor thrust and shaft torque from the medium mesh was plotted against time for the coarse and fine meshes for the rotor in sinusoidal surge motion in Figures 5 to 8.

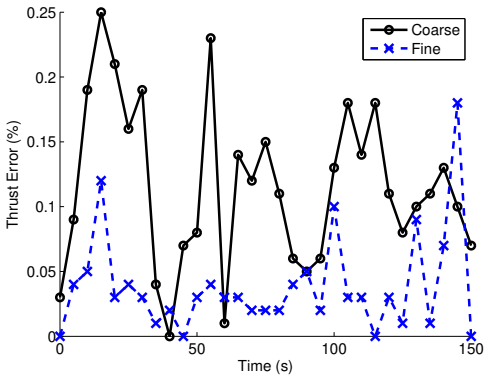

Figure 5: Percentage error in rotor thrust relative to medium mesh for sinusoidal surge motion with Amplitude=2m and Frequency=0.02Hz

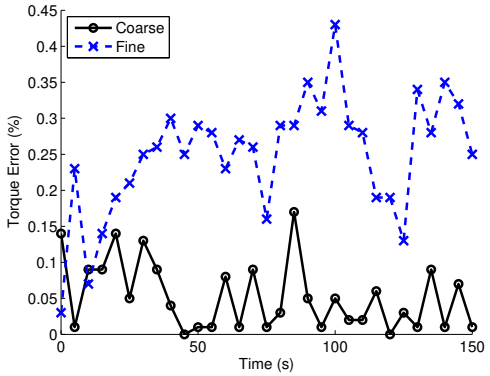

Figure 6: Percentage error in rotor shaft torque relative to medium mesh for sinusoidal surge motion with Amplitude=2m and Frequency=0.02Hz

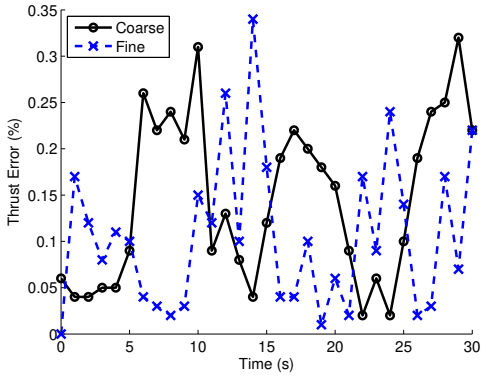

Figure 7: Percentage error in rotor thrust relative to medium mesh for sinusoidal surge motion with Amplitude=4m and Frequency=0.1Hz

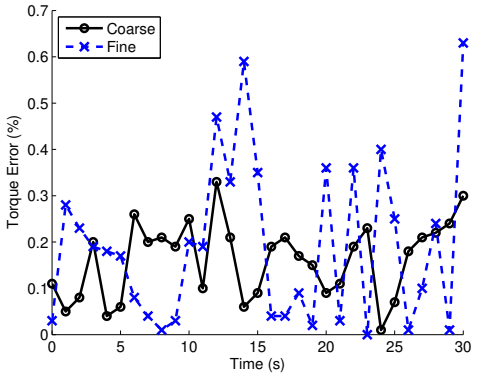

Figure 8: Percentage error in rotor shaft torque relative to medium mesh for sinusoidal surge motion with Amplitude=4m and Frequency=0.1Hz

All differences were less than 1% from the

medium mesh, and not proportional to the surge motion. Thus, the medium mesh was deemed acceptable for the study.

3.2.3 Time Step Refinement

A time step refinement study was conducted using the medium mesh. The fine time step was half the size of the medium time step, at 400 time steps per period, and the coarse time step was twice the size of the medium time step, at 100 time steps per period. The total thrust and shaft torque against time of the coarse and fine time steps were compared to the medium time step, and the percentage difference plotted in Figures 9 to 12.

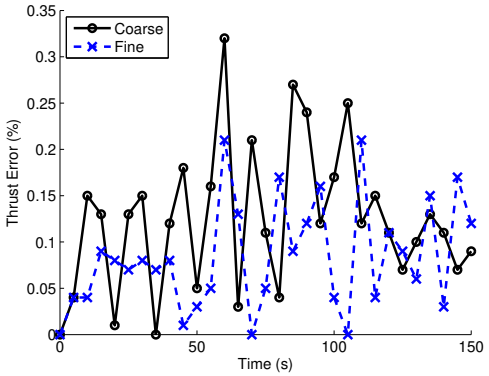

Figure 9: Percentage error in rotor thrust relative to medium time step for sinusoidal surge motion with Amplitude=2m and Frequency=0.02Hz

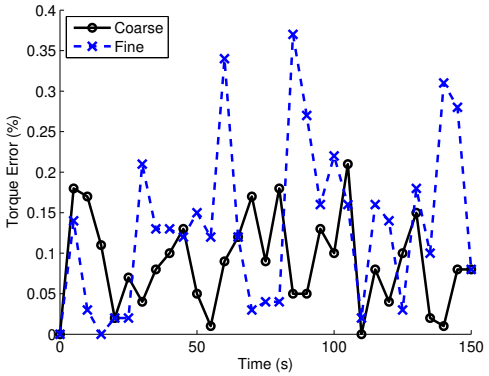

Figure 10: Percentage error in rotor shaft torque relative to medium time step for sinusoidal surge motion with Amplitude=2m and Frequency=0.02Hz

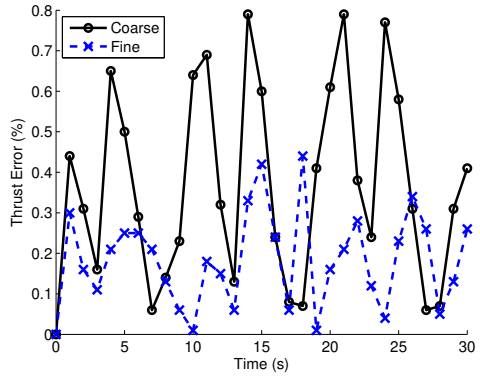

Figure 11: Percentage error in rotor thrust relative to medium time step for sinusoidal surge motion with Amplitude=4m and Frequency=0.1Hz

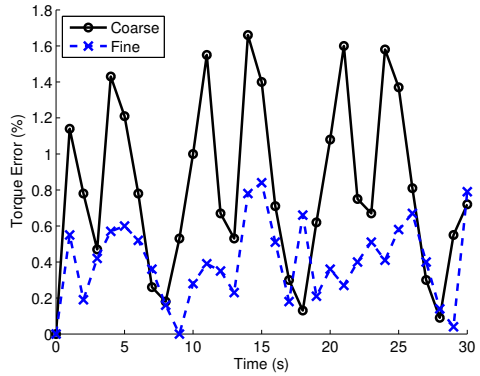

Figure 12: Percentage error in rotor shaft torque relative to medium time step for sinusoidal surge motion with Amplitude=4m and Frequency=0.1Hz

The results from Figures 9 to 12 indicate that the coarse time step had more than 1% difference from the medium time step, while the fine time step consistently had less than 1% difference. This suggests that the medium time step is refined enough to capture the transient flow phenomena.

3.3 Unsteady Blade Element Momentum Method

The unsteady blade element momentum method (uBEM) used in the present study, is based on the method presented in [12]. The relative velocity vector is given by:

$$\boldsymbol{V_{rel}} = \boldsymbol{V_0} + \boldsymbol{W} + \begin{pmatrix} 0 \\ -\Omega r \cos(\theta_c) \\ 0 \end{pmatrix} \tag{43}$$

where V_0 is the blade-specific wind speed at the blade element including relative speed due to rotor motion, Ω is the rotor rotational speed in rads^{-1}, r is the local blade segment radius. θ_c is the coning angle of the rotor, set to 0 radians for the present study.

The flow angle, ϕ, is the angle between the relative velocity and the normal of the rotor plane.

$$\phi = \arctan\left(\frac{V_{rel,y}}{V_{rel,z}}\right) \tag{44}$$

The normal (z) and tangential (y) induced velocities are then given by:

$$W_z = \frac{-|\boldsymbol{V_{rel}}|^2 C_l \cos(\phi)\, cB}{8F\left|(\boldsymbol{V_0}+\boldsymbol{A}) + f_g \begin{pmatrix} 0 \\ 0 \\ W_z \end{pmatrix}\right| \pi r} \tag{45}$$

$$W_y = \frac{-|\boldsymbol{V_{rel}}|^2 C_l \sin(\phi)\, cB}{8F\left|(\boldsymbol{V_0}+\boldsymbol{A}) + f_g \begin{pmatrix} 0 \\ 0 \\ W_z \end{pmatrix}\right| \pi r} \tag{46}$$

where B is the number of blades, F is the tip-loss factor, f_g is the Glauert correction for high axial induction factors and C_l is the coefficient of lift computed using the combined stall-delay and unsteady airfoil model at the angle of attack equal to the flow angle less the blade twist. W_x is set to 0.

At every time step, for each blade element in each blade, equations (43) to (44) are iterated until there is no change in the induced velocity vector. For the present study, this is set to a tolerance of 1e^{-5}

4 Results and Discussion

The changes in Λ (equation (5)) against time for the NREL 5MW wind turbine are shown in Figure 13 for the wind turbine in a sinusoidal surge motion with an amplitude of 6m and frequency of 0.5Hz.

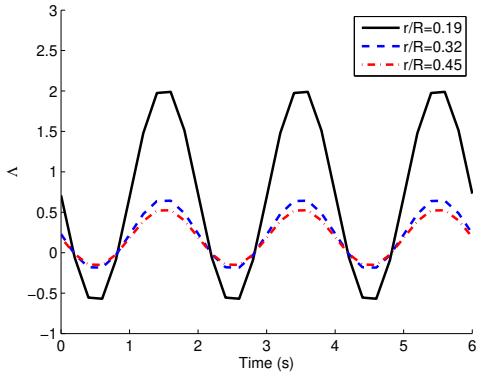

Figure 13: Lambda against time for different blade segments for rotor in surging motion with Frequency $= 0.5Hz$ and Amplitude $= 6m$

Figure 13 shows large periodic changes in Λ. This significant change in Λ will affect the degree of stall-delay on the local blade segment.

The coefficient of lift, C_L, is shown for elements at $r/R = 0.19$, $r/R = 0.58$ and $r/R = 0.71$ on the rotor, with a pre-treated stall delay and with a real-time stall delay, in Figures 14 to 16 respectively.

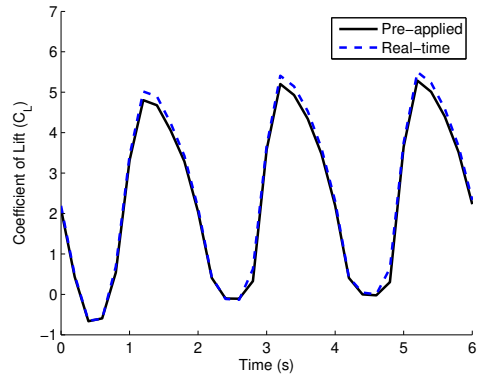

Figure 14: C_L against time for $r/R = 0.19$ for rotor in surging motion with Frequency $= 0.5Hz$ and Amplitude $= 6m$ using pre-applied and real-time stall-delay

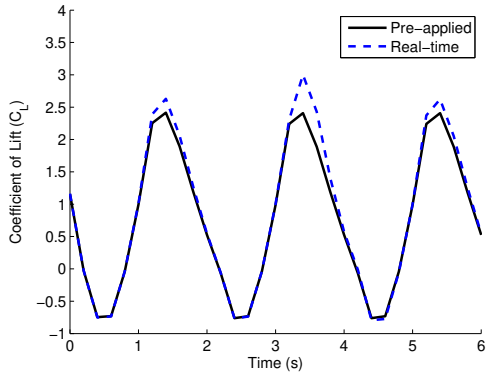

Figure 15: C_L against time for $r/R = 0.58$ for rotor in surging motion with Frequency $= 0.5Hz$ and Amplitude $= 6m$ using pre-applied and real-time stall-delay

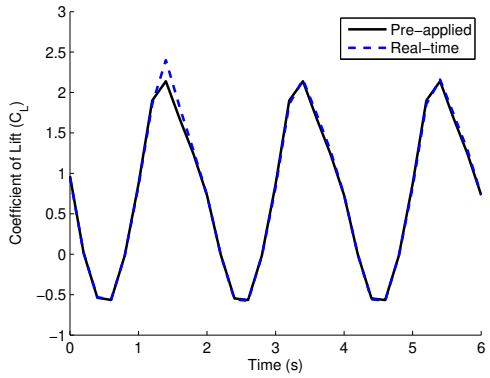

Figure 16: C_L against time for $r/R = 0.71$ for rotor in surging motion with Frequency $= 0.5Hz$ and Amplitude $= 6m$ using pre-applied and real-time stall-delay

Some highly significant differences in coefficient of lift are observed over the different blade segments, especially at the peaks. This implies that the prediction in real-time force distribution over the blade for structural analysis would be highly uncertain without a real-time stall delay implemented.

The rotor thrust and shaft torque are compared, with a pre-treated stall delay and with a real-time stall delay, in Figure 17.

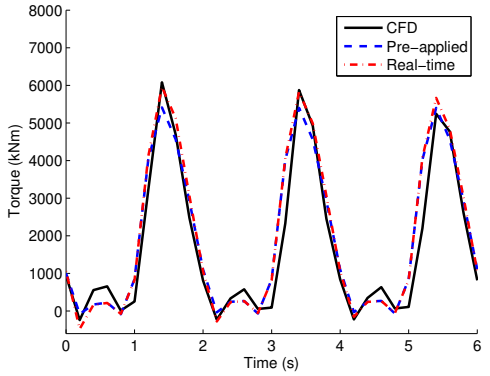

Figure 17: Predicted shaft torque against time for rotor in surging motion with Frequency $= 0.5Hz$ and Amplitude $= 6m$ using pre-applied and real-time stall-delay, compared to CFD

A 9% difference in accuracy of peak predicted shaft torque between the pre-applied stall-delay and real-time stall-delay compared to CFD is observed at the first peak. This would affect fatigue and power-prediction analyses for a FOWT.

5 Conclusion

The stall-delay model of Du & Selig [3] was combined with the airfoil-shape dependent modified Beddoes-Leishman model of Singapore Wala et al [4] to produce a model which simulates the motion of the boundary layer both due to changes in angle of attack and Coriolis effect with blade rotation.

The changes in speed ratio during the surging motion of a FOWT were demonstrated, which resulted in variation for coefficient of lift, and finally changes in rotor thrust and torque. It was shown that pre-application of a stall-delay model to airfoil aerodynamic data would not model the changes in stall-delay, thus, a real-time stall delay model is required that works in combination with an unsteady airfoil model for an accurate assessment of FOWT aerodynamics. In addition, a comparison of uBEM with the unsteady airfoil model versus uBEM with static aerodynamics tables shows increased accuracy in predicting the shaft torque, and better reflection of the distribution of thrust and shaft torque against time.

Future work may involve careful turbine-specific calibration of the stall-delay model to produce a greater degree of accuracy when assessing FOWT aerodynamics. This can be done through CFD studies using a wide-ranging simulation matrix. This combined model should also develop to eventually encompass unsteady tip-loss, to better reflect the flow physics of the wind turbine.

Disclaimer

The views expressed in this paper are those of the authors and do not necessarily reflect those of their affiliated companies and organisations.

Acknowledgements: The research was supported by the Singapore Economic Development Board (grant No. EDB-IPP-LR-JIP RCA-13/056).

References:

[1] H. Dumitrescu, C. Vladimir, and F. Frunzulica, "An insight into the rotational stall delay," *Proc. Appl. Math. Mech.*, vol. 12, no. 1, pp. 457–458, 2012.

[2] C. Zhu and T. Wang, "Comparative study of dynamic stall under pitch oscillation and oscillating freestream on wind turbine airfoil and blade," *Applied Sciences*, vol. 8, p. 1242, Jul 2018.

[3] Z. Du and M. Selig, "A 3-D stall-delay model for horizontal axis wind turbine performance prediction," in *1998 ASME Wind Energy Symposium*, (Reno, NV, USA), pp. 9–19, 1998.

[4] A. A. Singapore Wala, E. Y. K. Ng, and N. Srikanth, "A Beddoes-Leishman–type model with an optimization-based methodology and airfoil shape parameters," *Wind Energy*, vol. 21, no. 7, pp. 590–603, 2018.

[5] D. Hu, O. Hua, and Z. Du, "A study on stall-delay for horizontal axis wind turbine," *Renewable Energy*, vol. 31, pp. 821–836, May 2006.

[6] J. G. Leishman and T. S. Beddoes, "A generalised model for airfoil unsteady aerodynamic behaviour and dynamic stall using the indicial method," in *Proceedings of the 42nd Annual Forum of the American Helicopter Society*, (Washington DC, USA), pp. 243–266, 1986.

[7] A. Björck, "Dynstall: Subroutine and package with a and dynamic stall model," Tech. Rep. FFAP-V-110, Flygtekniska Frsöksanstalten, Bromma, Sweden, 2000.

[8] M. H. Hansen, M. Gauna, and H. A. Madsen, "A beddoes-leishman type dynamic stall model in state-space and indicial formulations," Tech. Rep. Risø-R-1354(EN), RisøNational Laboratory, Roskilde, Denmark, 2004.

[9] B. E. Thwaites, *Incompressible Aerodynamics*. Oxford, UK: Oxford University Press, 1960.

[10] R. B. S. Pereira, "Validating the Beddoes-Leishman dynamic stall model in the horizontal axis wind turbine environment," Master's thesis, Universidad Tecnica de Lisboa, 2010.

[11] A. A. Singapore Wala, *Aerodynamics Modelling of Floating Offshore Wind Turbines*. PhD Thesis, Nanyang Technological University, Singapore, May 2017.

[12] A. A. Singapore Wala, E. Y.-K. Ng, A. Bahuguni, and N. Srikanth, "Quantification and modelling of the dynamic wake effect for floating offshore wind turbines," in *Offshore Technology Conference*, (Houston, TX, USA), May 2017.